

Improved imaging with phase-weighted common conversion point stacks of receiver functions

A. Frassetto,^{1,2} G. Zandt,² H. Gilbert,³ T. J. Owens⁴ and C. H. Jones⁵

¹Department of Geosciences, University of Arizona, Gould-Simpson Building #77, 1040 E 4th St., Tucson, AZ 85721, USA

²Department of Geography and Geology, University of Copenhagen, Øster Voldgade 10, DK-1350 Copenhagen, Denmark.

E-mail: Af@geo.ku.dk

³Department of Earth and Atmospheric Sciences, Purdue University, 550 Stadium Mall Dr., West Lafayette, IN 47907, USA

⁴Department of Geological Sciences, University of South Carolina, 701 Sumter St., EWS 617, Columbia, SC 29208, USA

⁵Department of Geological Sciences, University of Colorado, Campus Box 399, 2200 Colorado Ave., Boulder, CO 80309-0399, USA

Accepted 2010 April 5. Received 2010 April 5; in original form 2009 November 30

SUMMARY

Broad-band array studies frequently stack receiver functions to improve their signal-to-noise ratio while mapping structures in the crust and upper mantle. Noise may produce spurious secondary arrivals that obscure or mimic arrivals produced by *P*-to-*S* conversions at large contrasts in seismic impedance such as the Moho. We use a Hilbert transform to calculate phase-weights, which minimize the constructive stacking of erroneous signal in receiver function data sets. We outline this approach and demonstrate its application through synthetic data combined with different types of noise, a previously published example of signal-generated noise, and a large data set from the Sierra Nevada EarthScope Project. These examples show that phase-weighting reduces the presence of signal-generated noise in receiver functions and improves stacked data sets.

Key words: Image processing; Interface waves; Site effects; Wave scattering and diffraction; Crustal structure.

1 INTRODUCTION

Receiver functions (e.g. Langston 1979) have become a standard means to measure the structure of the crust and upper mantle beneath a three-component broad-band seismometer. Vertical seismograms are deconvolved from the radial and tangential components to remove source and instrument effects. This preserves *P*-to-*S* conversions generated by an upgoing *P*-wave that encounters prominent subhorizontal discontinuities beneath a seismic station. Radial component receiver functions created for an array of seismometers may be combined into a 3-D volume and interpreted structurally. This process often utilizes common conversion point (CCP) stacking (Dueker & Sheehan 1997), which averages the amplitude of receiver functions from several station-event pairs that sample the same region of the subsurface. The procedure increases the signal-to-noise ratio through linear stacking and enhances laterally coherent structures such as the Moho or upper-mantle discontinuities.

Although receiver functions may appear simple in some cases, numerous studies document how common structural heterogeneities contaminate individual traces with a signal that arrives at higher incidence angles than the near-vertically incident conversions generated by subhorizontal structure (e.g. Abers 1998). Irregular topography along both the free-surface and the Moho induces considerable scattering of arrivals and influences the amplitude of the conversion from the Moho (Clouser & Langston 1995). Both Abers (1998) and Morozov (2004) demonstrate the coherency and high amplitude of

signal generated by dipping, out-of-plane, sedimentary structures. Despite the advent of advanced processing methods (e.g. Levander *et al.* 2005) and because array deployments rarely study uncomplicated targets, the effect of ‘signal-generated noise’ (i.e. scattering, reverberations, diffractions and azimuthally dependent signal) produced by topography, faults, sediments and anisotropy remains a significant concern when using receiver functions.

We adopt the phase-weighting algorithm developed by Schimmel & Paulssen (1997) to suppress spurious noise. Phase-weighting has been used in core–mantle boundary studies (Helffrich & Kaneshima 2004) and in H-K (depth– V_p/V_s domain) stacks of receiver functions (Crotwell & Owens 2005). Here a revised CCP method incorporates phase-weighting, and we highlight its application to both synthetic data and examples from the Geyokcha experiment (Abers 1998) in Turkmenistan and the Sierra Nevada EarthScope Project (SNEP), a broad-band deployment in the Sierra Nevada batholith in western North America (Gilbert *et al.* 2007).

2 PHASE-WEIGHTED STACKING

The phase-weighting scheme presented here builds on geographically stacking receiver functions into CCP bins. We therefore briefly describe the initial processing of the data contributing to the CCP stacks. Frassetto *et al.* (2010) provides a detailed overview of the procedure, which generally follows Gilbert *et al.* (2003) and Gilbert

& Sheehan (2004). We start by applying a wide bandpass to the seismograms (e.g. 0.15 to 5 Hz) and calculating receiver functions from impulsive teleseismic P and PP arrivals using an iterative method of time-domain deconvolution (Ligorria & Ammon 1999). We typically specify an a value of 2.5 for the width of the Gaussian spike, which serves as a low-pass filter with a corner of ~ 1.2 Hz. Using a one-fourth-wavelength calculation and assuming a wave speed of 4 km s^{-1} , receiver functions in this frequency range recover layer thicknesses greater than ~ 0.8 km. Some data may be discarded based on user-defined criteria discussed later, and the remaining traces are normalized so that the maximum amplitude of the zero-lag P -wave equals one. Amplitudes of P s phases are rescaled to account for the wide range of distances for events used. All receiver function amplitudes are multiplied by i_r/i , where i_r is a depth-invariant reference angle (20°) and i is the incidence angle calculated from the slowness of the P -wave for each receiver function (Jones & Phinney 1998).

Receiver functions are then migrated from time to depth, back-projected along their incoming ray paths and distributed into gridded bins. Migrated depths determined from receiver functions rely mostly on accurately constraining V_s and much less on V_p (Zandt *et al.* 1995). For SNEP we migrate using a model developed from teleseismic P -tomography at 40 km depth (Reeg *et al.* 2008) and V_p/V_s determinations from CCP receiver function stacks, local earthquake arrivals and petrologic modelling (Frassetto *et al.* 2010). This ensures the most accurate estimate of Moho depths that we can determine. For a model that assumes a typical crustal V_p of 6.2 km s^{-1} and $V_p/V_s = 1.7 \text{ km s}^{-1}$, a ± 2.5 per cent variation in V_p/V_s skews the migrated depth to a conversion at 40 km by about ± 2.5 km. To constrain uncertainty related to picking the migrated Moho, we estimate errors by performing 100 bootstrap resamplings (Efron & Tibshirani 1986) of the arrival depth of the Moho for each column of CCP stacking bins. We reject 33 per cent of estimates lying farthest from the median depth and for the remaining values calculate a standard deviation. The average value of the standard deviation is ~ 0.8 km across the SNEP array. For comparison, the width of the Gaussian pulse for $a = 2.5$ and a sharp discontinuity is ~ 1 s, which equates to 8 km when migrated using V_p of 6.2 km s^{-1} and $V_p/V_s = 1.7$. Errors of < 1 km are well inside the width of a typical conversion from the Moho and thus only produce a negligible reduction in the associated phase-weight.

The size and spacing of the bins used for stacking depend on the aperture and density of stations in the array. For SNEP, in which most stations are spaced 20–25 km apart, the bins are distributed along a $15 \text{ km} \times 15 \text{ km}$ grid and each has a horizontal radius of 20 km and vertical thickness of 0.5 km. The sampling area extends by 45 bins (675 km) in a NNW–SSE direction and 18 bins (270 km) in the ENE–WSW direction. We stack receiver functions between adjacent bins to enhance laterally coherent conversions and close gaps in data coverage caused by non-uniform station and event distribution. Bins are only kept if they contain at least 10 receiver functions. Stacking helps diminish azimuthal heterogeneities at shallow depths, and adjacent bins sampling the mid-to-upper crust are small enough to image lateral structural variations.

We then multiply the mean, linearly stacked receiver function for each bin with the sum of its correspondingly stacked instantaneous phases. The ideal result of this multiplication should be the reduction of amplitudes associated with incoherent arrivals (that correspondingly possess low phase-weights) and the preservation of coherent energy (which sum to high phase-weights). To accomplish this we compute the Hilbert transform of all receiver functions that sample each bin at each depth, to yield terms for amplitude and

instantaneous phase. Using notation modified from Schimmel & Paulssen (1997) this procedure can be expressed as:

$$S(z) = s(z) + iH(s(z)) = A(z)e^{i\Phi(z)}. \quad (1)$$

The term $S(z)$ represents the analytic signal or complex trace representing the depth-converted receiver function. The terms $s(z)$ and $H(s(z))$ define the real and imaginary components of that signal, where H is its Hilbert transform. The second formulation in eq. (1) represents $A(z)$ as the amplitude and $\Phi(z)$ as the instantaneous phase. The values of the instantaneous phase are summed and averaged to an absolute term

$$c(z) = \frac{1}{N} \left| \sum_{j=1}^N e^{i\Phi_j(z)} \right|, \quad (2)$$

where N is the number of receiver functions, and $c(z)$ represents the mean phase-weight for a particular depth, z . For each trace (j) amplitudes (s_j) are linearly weighted (w_j) as a function of distance from the bin centre, summed, and averaged using the standard CCP procedure and then multiplied by the phase-weighting term $c(z)$.

$$g(z) = \left[\frac{1}{N} \sum_{j=1}^N w_j s_j(z) \right] c(z)^v. \quad (3)$$

The weighting factor $c(z)$ (eq. 2) varies from 0 to 1 and can be applied directly, or modified by an exponential term (v) (eq. 3) to adjust the sharpness of the filter. A v value of 0 corresponds to linear stacking. Both the stacked amplitudes and the phase-weights can be smoothed using a multiple-point moving average, the vertical width of which can be adjusted depending on the scale of the targets of interest, noisiness of the data and tolerance for waveform distortion. Widths of an averaging function greater than a few kilometres tend to significantly reduce the maximum amplitude of prominent conversions by smearing the amplitudes.

3 SYNTHETIC TESTS

To evaluate the effectiveness of phase-weighting, we isolate true signal from synthetic CCP stacks with added noise. We model a 2-D structure, where the Moho dips 10° westwards over 160 km. The wave speed of the mantle half-space decreases westwards while the crust remains constant, decreasing the magnitude of the impedance contrast across the Moho (Fig. 1). We sample this structure at nine ‘stations’ spaced at 20 km intervals along the model and generate synthetic seismograms for an incident P -wave and its primary P -to- S conversion over a range of ray-parameters ($0.04, 0.05, 0.06, 0.07$ and 0.08 s km^{-1}) and backazimuths (30° increments) using the ray tracing code *ray3d* (Owens *et al.* 1984). For replicating spurious arrivals in the receiver functions, we separately add two different types of noise to the synthetic waveforms before deconvolution: random records of microseismic and cultural noise from seismically quiet intervals at SNEP stations and a synthetic S wave travelling eastwards across the model. The S wave is generated using the reflection-matrix reflectivity code *mijkennett* (Randall 1994) for a 10-km-deep source located 20 km from the westernmost station. The moment tensor is strike-slip and oriented 45° oblique to the model, the maximum frequency of the wave is capped at 5 Hz, and Q_p is reduced to effectively zero. We calculate each synthetic seismogram through a narrow range of slowness (0.025 – 0.04 s km^{-1}) to obtain the desired moveout of the phase. These parameters restrict

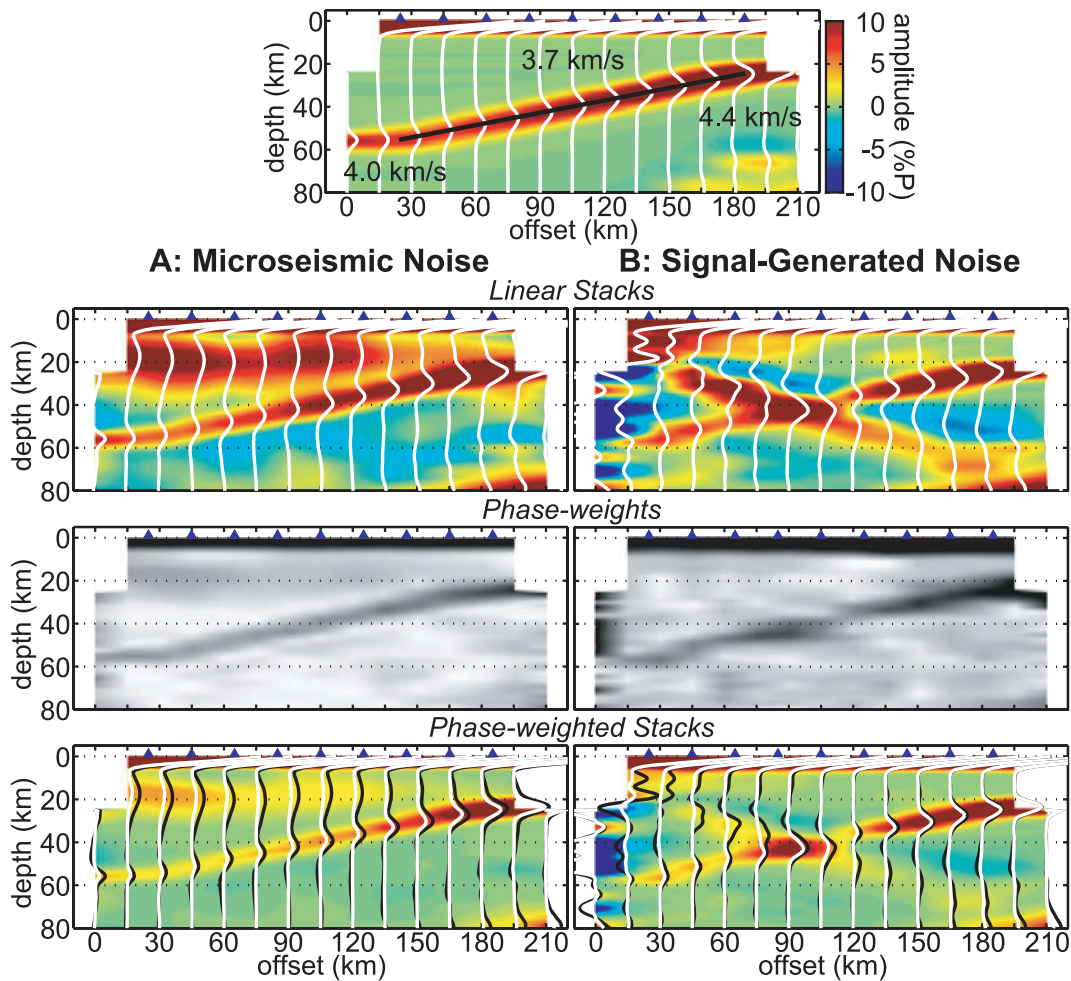


Figure 1. Synthetic receiver function stacks for a 2-D model of the Moho dipping 10° westwards (top). The crust remains homogenous while the P -wave speed and S -wave speed of the upper mantle decrease westwards. Shear wave speed values are displayed. Column A shows stacks with microseismic noise. Column B shows stacks with signal-generated noise. Each example shows the linear stack with no phase-weighting, the calculated phase-weights ($v = 1$), and the stack with weights applied. The phase-weighted stacks contain both the linear receiver function stack for each bin (black) and the phase-weighted (white). Phase-weights emphasize coherent arrivals, and range between 0 (white) and 1 (black).

the output to an impulsive, single phase S wave that is calculated for the corresponding stations used to calculate the synthetic receiver functions.

Amplitude and frequency differ for these respective sets of noise; records at SNEP stations vary in amplitude by several hundred counts and have a dominant frequency characteristic of oceanic microseism (e.g. Oliver & Page 1963). Synthetic seismograms from *mijkennett* show a main arrival with a single cycle of ~ 1 Hz and minor high-frequency energy which results from the restricted frequency-slowness window of the synthetic. These arrivals are only decimal scale. Therefore we rescale each set of noise to avoid it obscuring or being hidden by the output from *ray3d*. Microseismic noise is reduced to impart signal-to-noise ratios of ~ 1 – 10 . Tests on these synthetics show that the iterative deconvolution becomes increasingly ineffective for lower signal-to-noise ratios. The S -arrival in the *mijkennett* output diminishes moving eastwards and is boosted to match the approximate amplitudes of the *ray3d* conversions. Microseismic noise recorded by SNEP stations is distributed randomly to each *ray3d* seismogram, while the synthetic S -arrivals are added systematically to each station at its appropriate time for events from western backazimuths (240° , 270° and 300°). The com-

bined signals are visually inspected to ensure that the original P -to- S conversions are discernable and then deconvolved into receiver functions. We follow the same steps for processing real waveforms; filtering the seismogram, using $a = 2.5$ as a Gaussian low-pass filter, normalizing the maximum amplitude on each trace, rescaling the amplitudes to the appropriate incidence angle, migrating to depth and stacking.

The added noise remains in the synthetic data following receiver function calculation and linear CCP stacking (Fig. 1). While signal from the original Moho arrives clearly in both examples of noise, the noise adds several other prominent arrivals. This is particularly true for the example of ‘signal-generated noise’, which appears clearly despite being present in only one fourth of the synthetic seismograms. The calculation of phase-weights for $v = 1$ emphasizes only the dipping Moho and corresponding phase-weighted stacks eliminate nearly all spurious arrivals. Although the excessive noise and phase-weighting does diminish the amplitude of the signal, the true structure is clearly resolved across the entire model. Because of distortions to CCP amplitudes with phase-weighting, it is important to consider amplitudes from linear stacking when modelling structures observed in actual data.

4 APPLICATION TO DATA

4.1 Geyokcha array

Deployed to study local seismicity and site response along the Kopet Dagh Mountains in southern Turkmenistan, the Geyokcha array recorded an event that produced a notable example of signal-generated noise in receiver functions (Abers 1998). Instead of detecting a static conversion from the Moho produced at its expected depth, 12 stations spaced at ~ 250 m capture the moveout of a high-amplitude phase with positive to negative to positive polarities arriving between 3.5 and 5.5 s after the P wave and travelling across the array at $2.5\text{--}3.0$ km s^{-1} (Fig. 2). This phase remains consistent for multiple events and backazimuths suggesting that it emanates from a shallow source. Abers (1998) inverted for the location of this phase and concluded that a range-bounding fault to the north of the Geyokcha array generates high amplitude, near-surface scattering that obscures the arrival of the P -to- S converted phase from the Moho when viewed at a single station.

To demonstrate the effects of phase-weighted stacking on these data that possess signal-generated noise, we calculate receiver functions for the example event presented in this study and stack the traces with and without phase-weighting (Fig. 3). Because of the non-uniform spacing between the stations, we select only the evenly spaced first, middle and last stations that record the scattered arrival and stack them together in the time domain (Fig. 2). The linear stack enhances the overall signal-to-noise ratio, but leaves intact a large portion of the negatively polarized scattered energy between 4 and 5 s at both higher and lower frequencies (Fig. 3). In contrast, phase-weighted stacks nearly eliminate this scattered energy and preserve both early and late coherent arrivals that presumably relate to conversions from true structure. We similarly evaluate all stations for this event, but the higher density of observations between 0 and 1 km distance increases the phase-weights for the spurious arrival by boosting the coherency between adjacent traces (Fig. 2). This is because the wavelength of the arrival, even for a narrow Gaussian, is significantly larger than the relatively small spacing between stations. As originally demonstrated by Schimmel & Paulssen (1997), the moveout of a phase primarily controls its phase-weight.

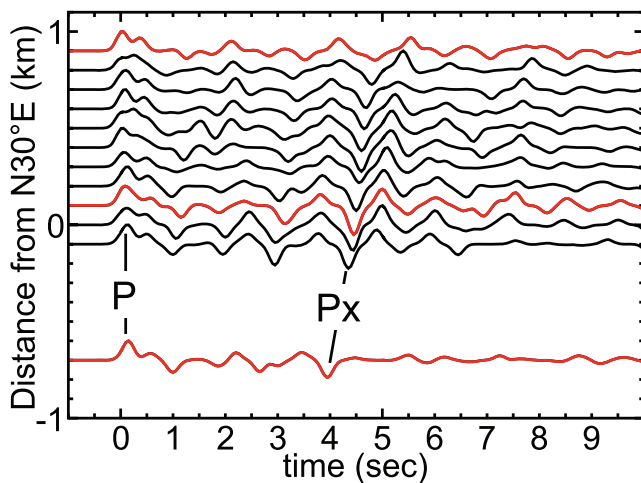


Figure 2. Record section showing the moveout of the scattered P_x phase recorded by the stations within the Geyokcha array on $a = 6.7$ receiver functions, after Abers (1998). The highlighted receiver functions (red) are stacked together in the example presented here using phase-weighting.

The overall adjustment in amplitudes from phase-weighting can be observed by plotting the absolute value of the difference between the linear stack and its phase-weighted version as a function of time. Peaks of the ‘residual’ highlight the arrivals which phase-weighting impacts most significantly (Fig. 3). For both $a = 2.5$ and $a = 6.7$, residuals ≥ 0.1 occur at approximately 2, 3, 4.5, 5.5 and 7 s. The largest residual occurs at 4.5 s at the centre of the prominently scattered arrival. The other residuals likely correspond to similar, though less energetic occurrences of noise. Phase-weighting removes negative arrivals that could otherwise erroneously be interpreted as lamination above and below the Moho, which appears clearly at ~ 5.5 s. On stacks for both a -values, we interpret shallow structures based on negative arrivals at 1 to 3 s and a two-stage crust–mantle transition represented by a positive coherent arrival at 7.5 s with amplitude equal to the earlier phase interpreted as Moho. While the effective suppression of noise for $a = 2.5$ demonstrates the utility of phase-weighting at frequencies used in teleseismic studies, greater improvement using a larger a -value shows the potential of phase-weighting higher frequency data sets.

4.2 Sierra Nevada EarthScope Project

We analysed 15 646 receiver functions generated from 69 520 teleseismic P - and PP -arrivals recorded at 166 broad-band seismometers across the Sierra Nevada, including 90 deployed in the central and northern Sierra from 2005 May to 2007 September as part of SNEP. To assemble this data set, we use events with a signal-to-noise ratio > 2 , and accept receiver functions if they fit at least 80 per cent of the signal during deconvolution. Additionally we only keep receiver functions that exhibit waveform qualities consistent with the expected response for a receiver function: the normalized maximum amplitude equals 1 near zero-lag, negative amplitudes do not exceed -1 , and the direct P is not preceded by a negative trough or significant delay. Additional spurious data were removed after visual inspection, and in several cases specific backazimuths or entire stations were removed due to the presence of excessive harmonic oscillation. The average CCP bin at 40 km depth stacks ~ 106 receiver functions and contains a mean variance reduction of 90.5 per cent, demonstrating the high fold of data and robustness of the iterative deconvolution process.

An appraisal of linearly stacked data illustrates the need to consider noise-reduction practices even for high-quality, densely sampled data sets. While SNEP receiver functions stacked with $v = 0$ produce images with coherent features in the crust and upper mantle, they also contain less-coherent secondary arrivals (Figs 4 and 5). In the west-central Sierra foothills (Fig. 4 [B-B’: offset 15–105]) a negative conversion at 10–15 km depth signifies an apparent decrease in wave speeds within the crust. However, detailed controlled-source studies in this region measure no zone of low wave speed significant enough to be observed in a receiver function (Fliedner *et al.* 2000). These types of arrivals need to be further investigated.

The source of signal-generated noise here likely results from the complicated geologic and tectonic setting. Whereas relatively homogenous granitoid plutons underlie much of the southern and central Sierra Nevada, the northern section of the range and its boundaries are a combination of Mesozoic-age arc-related plutons, Cenozoic-age volcanic cover extensional grabens and related recent sedimentation along the border with the Basin and Range, metamorphosed ophiolites and sediments in the western foothills and the massive Great Valley forearc basin (e.g. Christensen 1966; Ducea 2001). This diversity of crustal constituents, steeply dipping

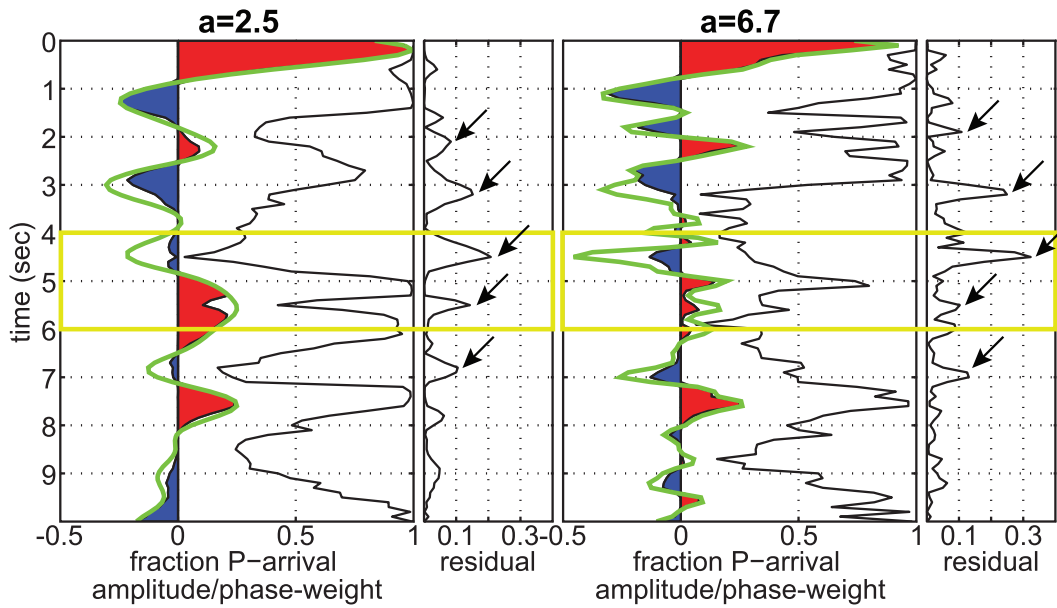


Figure 3. Phase-weighted stacks for receiver functions using $a = 2.5$ and $a = 6.7$ generated from the example in Abers (1998). A green line represents the linearly stacked receiver function whereas a black line shows the value of phase-weights at specific time. Corresponding to each stack, the phase-weighting residual presents the absolute value of the difference between the linear and phase-weighted amplitudes. Yellow boxes highlight the range of arrival-times for the scattered phase between 4 and 6 s. Arrows identify prominent peaks in the residual, highlighting zones of reduced noise.

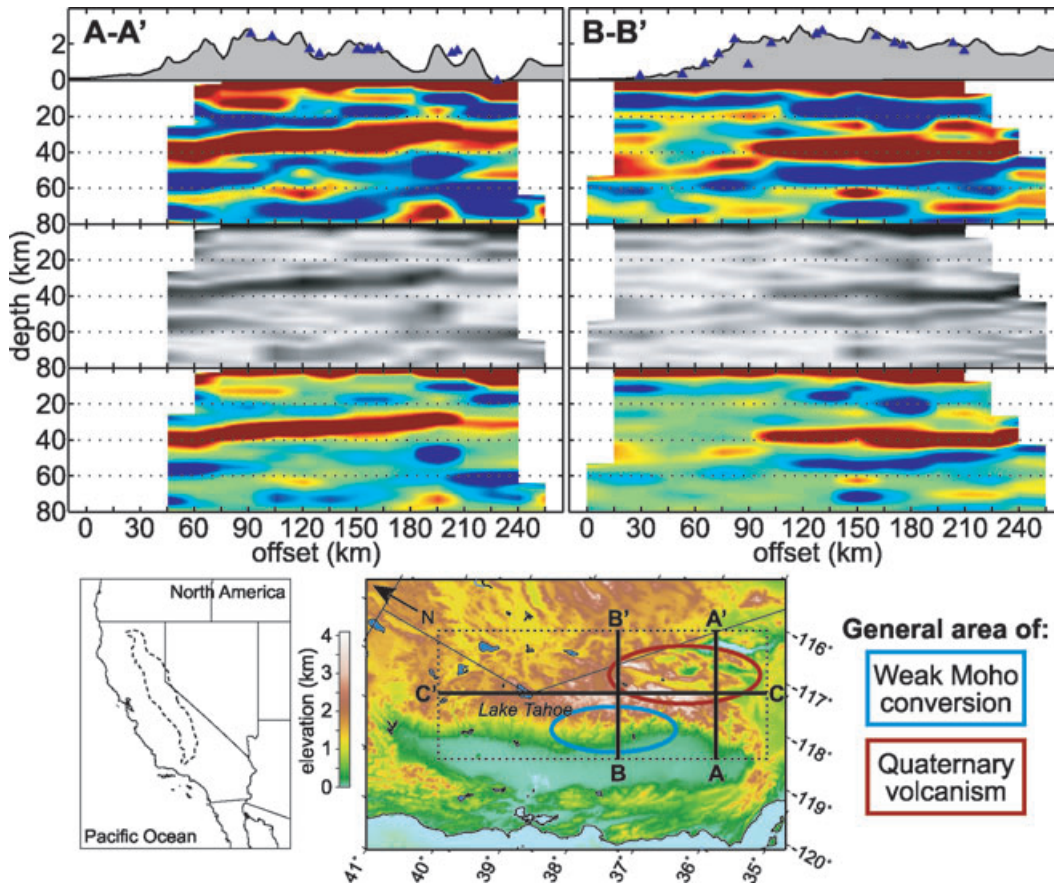


Figure 4. Linear stacks (top), phase-weights [ranging between 0 (white) and 1 (black)] (middle) and phase-weighted ($v = 1$) stacks (bottom) for transects A-A' and B-B' from SNEP. Reference maps show location of study area, outline of the Sierra Nevada, and CCP transects for these profiles. Colour scale included in Fig. 1.

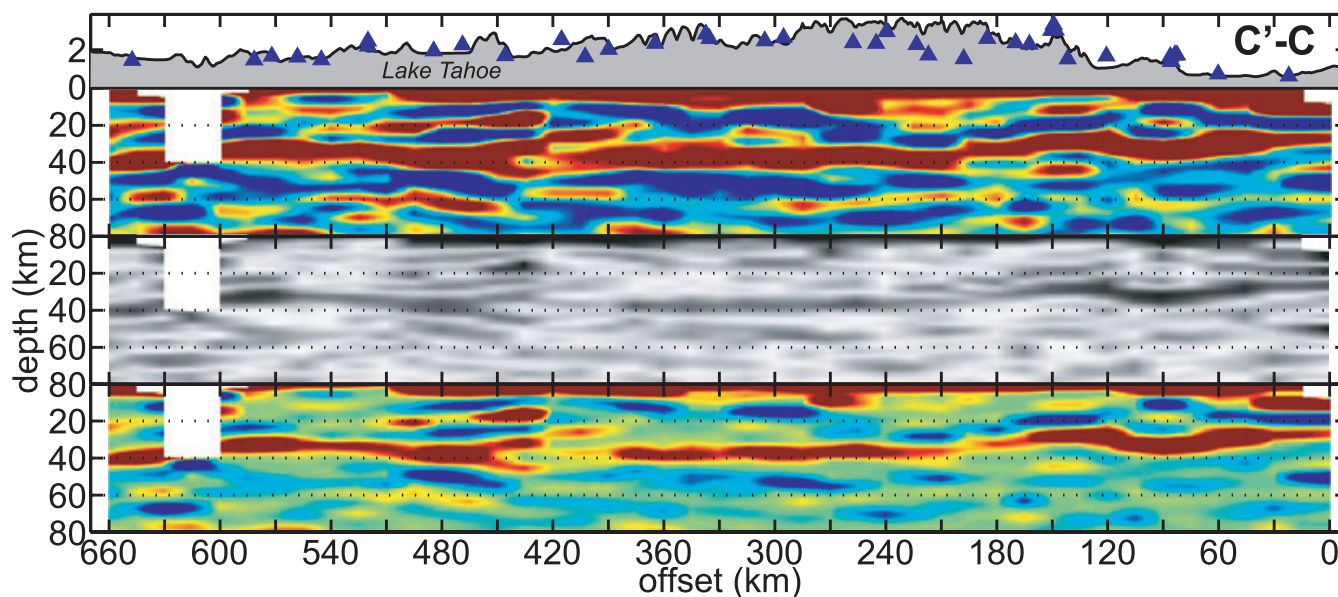


Figure 5. Linear stacks (top), phase-weights [ranging between 0 (white) and 1 (black)] (middle) and phase-weighted ($v = 1$) stacks (bottom) for transect C-C' from SNEP. Reference map located in Fig. 4.

structures observed within the foothills (Miller & Mooney 1994), the normal faulted escarpment of the eastern Sierra and high relief throughout the range all represent potential scattering points for the teleseismic wavefield.

We stack and phase-weight SNEP receiver functions for $v = 1$ and use a seven-point (or, 3.5 km width) moving average to smooth high-frequency signals created by the phase-weighting. Comparing phase-weighted and linear stacks demonstrates that the procedure dampens some weak arrivals, but keeps coherent features, providing greater confidence while interpreting regional variations in lithospheric structure. The Moho remains clearly defined throughout the southern and eastern Sierra, but dims to the west at 45–50 km depth [Fig. 4 (B-B': offset 0–90)]. Initial linear stacks in the western foothills resolved only a weak conversion from the Moho, and these amplitudes are reduced slightly by the phase-weighting. Additionally, the distribution of negatively polarized arrivals changes after phase-weighting, limiting these features to the eastern half of SNEP near several Quaternary volcanic fields (e.g. Manley *et al.* 2000) [Fig. 4 (A-A': offset 180–240, B-B': offset 120–195)]. If real, these 'bright spots' would represent conversions from the top of low wave speed layers and may signify the presence of partial melt.

Despite the overall improvement of the phase-weighted stacks some evidence of high-amplitude reverberations or scattering remains in the data set. Receiver functions calculated from data recorded near Lake Tahoe contain extremely energetic P -codas which likely result from scattering related to local structure [Fig. 5 (C-C': offset 480)]. While increasing the phase-weighting parameter may further dampen this energy, the likelihood of removing true signal becomes a concern. Thus, a trade-off exists in phase-weighting between noise suppression and loss of signal. Choice of an appropriate phase-weighting value varies with the amount and quality of data, sampling rate, a -value, bin size and sharing parameters, and amount of geologic complexity within the survey region.

Although a detailed geologic interpretation is not our objective here, the phase-weighting procedure helps to address the main motivations of SNEP (Gilbert *et al.* 2007); discerning the distribution of mafic–ultramafic residue produced by the Mesozoic-age batholith

in the central Sierra Nevada, and constraining how its potential removal relates structurally or genetically to the recent observed volcanism in eastern California (Zandt *et al.* 2004). In regions where the Moho is weak or absent, we can infer a gradational increase in wave speed between the crust and mantle. The gradual, compositional change in this lithospheric column from felsic upper crust to mafic and ultramafic lower crust and upper mantle observed in local xenoliths supports this interpretation (Ducea 2001). Recent modelling of receiver functions from the analogous Coast Mountains Batholith shows how the amplitude of the conversion from the Moho directly relates to the constituents of the lower crust and upper mantle (Calkins *et al.* 2010). Where the Moho conversion remains pronounced and underlain by decrease in wave speed, it appears that the batholithic root has foundered and been replaced with hot, buoyant asthenosphere. Partial melting triggered by the upwelling asthenosphere may create layers of low wave speed in the crust and upper mantle, causing the bright spots restricted to the eastern side of the SNEP array and potentially sourcing young magmas erupted in the eastern Sierra (Manley *et al.* 2000).

5 CONCLUSIONS

Phase-weights reduce occurrences of spurious arrivals in CCP stacks of teleseismic receiver functions. The technique retrieves the true converted wave structure in stacks of noisy synthetic data and significantly reduces incoherent arrivals in observed data. For the Geyokcha array, phase-weighting removes much of the high-amplitude scattering generated by local structure, and improves the resolvability of shallow structure and the Moho. For the SNEP data set, phase-weighting clarifies the boundaries of between where the Moho produces a strong and weak conversion, and highlights bright spots in the crust and upper mantle that may result from the presence of partial melt. These observations help demarcate the boundary of foundered lithosphere beneath the Sierra Nevada. Experimenting with different phase-weights and comparing to linear stacks provides an excellent framework for understanding and significantly reducing the noise content in stacked receiver functions.

ACKNOWLEDGMENTS

We thank everyone involved in SNEP for their help in the installation, servicing, redeployment and data archiving of this seismic array. We are especially grateful to the many private landowners and public officials who generously provided us with permission to deploy our seismic equipment on their land. We thank Jeannot Trampert and Hanneke Paulssen for reviews, which improved the manuscript. Standing Order for Data (Owens *et al.* 2004) and Seismogram Transfer Program were used to collect seismograms used in this study. We used additional code written by Josh Calkins. Several figures were generated with the GMT package (Wessel & Smith 1991). The facilities of the IRIS Data Management System, and specifically the IRIS Data Management Center, were used for access to waveform and metadata required in this study. Data from the TA network were made freely available as part of the EarthScope US Array facility supported by the National Science Foundation, Major Research Facility program under Cooperative Agreement EAR-0350030. Global Seismographic Network (GSN) is a cooperative scientific facility operated jointly by the Incorporated Research Institutions for Seismology (IRIS), the United States Geological Survey (USGS) and the National Science Foundation (NSF). The IRIS DMS is funded through the National Science Foundation and specifically the GEO Directorate through the Instrumentation and Facilities Program of the National Science Foundation under Cooperative Agreement EAR-0552316. This work was supported by the National Science Foundation's EarthScope grants EAR-0454554, EAR-0454524 and EAR-0454535 to the Universities of Arizona, Colorado and South Carolina. This work was also made possible by funding from the National Science Foundation through the Graduate Research Fellowship Program.

REFERENCES

- Abers, G.A., 1998. Array measurements of phases used in receiver-function calculations: importance of scattering, *Bull. seism. Soc. Am.*, **88**, 313–318.
- Calkins, J.A., Zandt, G., Girardi, J., Dueker, K., Gehrels, G.E. & Ducea, M.N., 2010. Characterization of the crust of the Coast Mountains Batholith, British Columbia, from *P* to *S* converted seismic waves and petrologic modeling, *Earth planet. Sci. Lett.*, **289**, 145–155, doi:10.1016/j.epsl.2009.10.037.
- Christensen, M.N., 1966. Late Cenozoic crustal movements in the Sierra Nevada of California, *Geol. Soc. Am. Bull.*, **77**, 163–181.
- Clouser, R.H. & Langston, C.A., 1995. Effect of sinusoidal interfaces on teleseismic *P*-wave receiver functions, *Geophys. J. Int.*, **123**, 541–558.
- Crotwell, H.P. & Owens, T.J., 2005. Automated receiver function processing, *Seismol. Res. Lett.*, **76**, 702–709.
- Ducea, M.N., 2001. The California arc: thick granitic batholiths, eclogitic residues, lithospheric-scale thrusting, and magmatic flare-ups, *GSA Today*, **11**, 4–10.
- Dueker, K.G. & Sheehan, A.F., 1997. Mantle discontinuity structure from midpoint stacks of converted *P* to *S* waves across the Yellowstone hotspot track, *J. geophys. Res.*, **102**, 8313–8327.
- Efron, B. & Tibshirani, R., 1986. Bootstrap methods for standard errors, confidence intervals, and other measures of statistical accuracy, *Statist. Sci.*, **1**, 54–77.
- Fliedner, M.M., Klemperer, S.L. & Christensen, N.I., 2000. Three-dimensional seismic model of the Sierra Nevada arc, California, and its implications for crustal and upper mantle composition, *J. geophys. Res.*, **105**, 10 899–10 921.
- Frassetto, A., Zandt, G., Gilbert, H., Owens, T.J. & Jones, C.H., 2010. Lithospheric structure of the Sierra Nevada from receiver functions and implications for lithospheric foundering, *Geosphere*, submitted.
- Gilbert, H.J., Sheehan, A.F., Dueker, K.G. & Molnar, P., 2003. Receiver functions in the western United States, with implications for upper mantle structure and dynamics, *J. geophys. Res.*, **108**, 2229, doi:10.1029/2001JB001194.
- Gilbert, H.J. & Sheehan, A.F., 2004. Images of crustal variations in the intermountain west, *J. geophys. Res.*, **109**, B03306, doi:10.1029/2003JB002730.
- Gilbert, H., Jones, C., Owens, T.J. & Zandt, G., 2007. Imaging Sierra Nevada lithospheric sinking, *Eos Trans. Am. geophys. Un.*, **88**(21), 225.
- Helffrich, G. & Kaneshima, S., 2004. Seismological constraints on core composition from Fe–O–S liquid immiscibility, *Science*, **306**, 2239–2242.
- Jones, C.H. & Phinney, R.A., 1998. Seismic structure of the lithosphere from teleseismic converted arrivals observed at small arrays in the southern Sierra Nevada and vicinity, California, *J. geophys. Res.*, **103**, 10 065–10 090.
- Langston, C.A., 1979. Structure under Mount Rainier, Washington, inferred from teleseismic body waves, *J. geophys. Res.*, **84**, 4749–4762.
- Levander A., Niu, F. & Symes, W.W., 2005. Imaging teleseismic *P* to *S* scattered waves using the Kirchhoff integral, in *Seismic Earth: Array Analysis of Broadband Seismograms*, pp. 149–169, eds. Levander, A. & Nolet, G., AGU Geophysical Monograph 157, doi:10.1029/156GM10.
- Ligorria, J. & Ammon, C.J., 1999. Iterative deconvolution of teleseismic seismograms and receiver function estimation, *Bull. seism. Soc. Am.*, **89**, 1395–1400.
- Manley, C.R., Glazner, A.F. & Farmer, G.L., 2000. Timing of volcanism in the Sierra Nevada of California: evidence for the Pliocene delamination of the batholithic root? *Geology*, **28**, 811–814.
- Miller, K.C. & Mooney, W.D., 1994. Crustal structure and composition of the southern Foothills Metamorphic Belt, Sierra Nevada, California, from seismic data, *J. geophys. Res.*, **99**, 6865–6880.
- Morozov, I.B., 2004. Crustal scattering and some artifacts in receiver function images, *Bull. seism. Soc. Am.*, **94**, 1492–1499.
- Oliver, J. & Page, R., 1963. Concurrent storms of long and ultra-long period microseisms, *Bull. seism. Soc. Am.*, **53**, 15–26.
- Owens, T.J., Zandt, G. & Taylor, S.R., 1984. Seismic evidence for an ancient rift beneath the Cumberland plateau, Tennessee: a detailed analysis of broadband teleseismic *p* waveforms, *J. geophys. Res.*, **89**, 7783–7795.
- Owens, T.J., Crotwell, H.P., Groves, C. & Oliver-Paul, P., 2004. SOD: standing order for data, *Seismol. Res. Lett.*, **75**, 515–520.
- Randall, G.E., 1994. Efficient calculation of complete differential seismograms for laterally homogenous earth models, *Geophys. J. Int.*, **118**, 245–254.
- Reeg, H., Jones, C.H., Gilbert, H., Owens, T.J. & Zandt, G., 2008. Tomographic observations connecting convective downwellings with lithospheric source regions, Sierra Nevada, California, *Eos Trans. Am. geophys. Un.*, **89**(53), Fall Meet. Suppl., Abstract S32B-06.
- Schimmel, M. & Paulssen, H., 1997. Noise reduction and detection of weak, coherent signals through phase-weighted stacks, *Geophys. J. Int.*, **130**, 497–505.
- Wessel, P. & Smith, W.H.F., 1991. Free software helps map and display data, *Eos Trans. AGU*, **82**, 441.
- Zandt, G., Myers, S.C. & Wallace, T.C., 1995. Crust and mantle structure across the Basin and Range–Colorado Plateau boundary at 37° N latitude and implications for Cenozoic extensional mechanism, *J. geophys. Res.*, **100**, 10 529–10 548.
- Zandt, G., Gilbert, H., Owens, T.J., Ducea, M., Saleeby, J. & Jones, C.H., 2004. Active foundering of a continental arc root beneath the southern Sierra Nevada in California, *Nature*, **431**, 41–46.